coatings

MDPI

Article

In Situ Fabrication of Ti-xNb Alloys by Conventional Powder Metallurgy

Rogelio Macias, Jr. [1], Pedro Garnica González [2], Luis Olmos [1,*], Ivon Alanis-Fuerte [1], Omar Jimenez [3], Francisco Alvarado-Hernández [4], Melina Velasco-Plascencia [2] and Jorge Alejandro Ávila-Olivera [1]

1 Instituto de Investigaciones en Ciencias de la Tierra, Universidad Michoacana de San Nicolas de Hidalgo, Morelia 58060, Mexico; jr.cach1m@gmail.com (R.M.J.); ivon.alanis.91@hotmail.com (I.A.-F.); alejandro.avila@umich.mx (J.A.Á.-O.)
2 División de Estudios de Posgrado e Investigación, Tecnológico Nacional de México/I.T. Morelia, Av. Tecnológico #1500, Colonia Lomas de Santiaguito, Morelia 58120, Mexico; p.garnica@itmorelia.edu.mx (P.G.G.); melina.vp@morelia.tecnm.mx (M.V.-P.)
3 Departamento de Ingeniería de Proyectos, Universidad de Guadalajara, Zapopan 45100, Mexico; omar.aleman@academicos.udg.mx
4 Unidad Académica de Ingeniería I, Universidad Autónoma de Zacatecas, Zacatecas 98000, Mexico; ingenierofah@uaz.edu.mx
* Correspondence: luis.olmos@umich.mx

Abstract: The present study shows the effect of Nb on a Ti matrix to fabricate composites via the conventional powder metallurgy for medical applications. Ti powder mixture compacts with different Nb contents were obtained from the conventional pressing and sintering technique. The sintering behavior was evaluated using the dilatometry technique, and the microstructure was studied using scanning electron microscopy (SEM) and X-ray diffraction (XDR). The mechanical properties were obtained from simple compression tests, and the corrosion resistance was determined from a standard three-electrode arrangement in Hank's solution. The results showed that the Nb in the Ti matrix limits the evolution of sintering depending on the Nb content. Nb slightly accelerates the phase transition temperature. The microstructure and X-rays revealed that biphasic α + β-Ti structures can be obtained, in addition to retaining the β-Ti phase and forming the martensitic phases α′ and α″ of Ti. Likewise, the mechanical behavior showed a Young's modulus of 10–45 GPa, which is close to that reported for human bones. Furthermore, the circuit analysis revealed that the Ti-Nb sintered systems were conditioned by the surface oxide layer and that the oxide layer formed within the residual pores of the sintering process. Finally, it was demonstrated that adding Nb to the Ti matrix increases the corrosion resistance and that contents close to 15 wt.% of this element have the best results.

Keywords: sintering; Ti alloys; mechanical properties; corrosion; biomedical applications

Citation: Macias, R., Jr.; Garnica González, P.; Olmos, L.; Alanis-Fuerte, I.; Jimenez, O.; Alvarado-Hernández, F.; Velasco-Plascencia, M.; Ávila-Olivera, J.A. In Situ Fabrication of Ti-xNb Alloys by Conventional Powder Metallurgy. *Coatings* **2024**, *14*, 897. https://doi.org/10.3390/coatings14070897

Academic Editors: Oleg Shichalin, Marcello Filgueira and Izabel Fernanda Machado

Received: 21 June 2024
Revised: 10 July 2024
Accepted: 15 July 2024
Published: 18 July 2024

1. Introduction

Recent research on metallic biomaterials has focused on Ti-based alloys composed of nontoxic elements such as Nb, Ta, Mo, Hf, and Zr to overcome the problems generated by the release of toxic metal ions in long-term implants [1,2]. There are several problems in addition to toxicity, one of which is the stress shielding phenomenon, which is defined as insufficient loading of the bone due to the difference in elastic modulus between the artificial device and adjacent bone tissues [3,4].

The ideal material or combination of materials for an implant should have, among others, the following properties: biocompatible chemical composition, good corrosion resistance, mechanical strength similar to that of human bones, low modulus to minimize bone resorption and a high wear resistance to minimize waste generation [5,6]. Additionally, the Ti-6Al-4V alloy has raised concerns due to the release of aluminum (Al) and vanadium (V) ions, which can be harmful to cells and tissues in the long term [7,8]. Therefore, it is

necessary to develop Ti-based components with low elastic moduli and optimum strength for medical use.

Titanium is an excellent metallic material due to its combination of properties, such as low density, relatively low modulus, excellent biocompatibility and good corrosion resistance [9,10]. New Ti alloys containing Nb, Ta, Mo and Zr have been developed for biomedical applications [11–13]; these alloys possess low moduli in the range of 55–85 GPa, which are higher than those reported for human bones (10–28 GPa) [3,14]. Porous materials generate a three-dimensional matrix of interconnected porosity, and porosity is necessary for bone fixation and growth [15,16]. The conventional powder metallurgy technique (PM) [17] has been shown to help in obtaining pieces with interparticle porosity by controlling the particle size and sintering temperature [18]. In spark plasma sintering (SPS), the control of porosity and mechanical properties is more complicated than with the PM technique [19]. Additionally, the porosity favors obtaining a low Young's modulus close to that of human bone [14,20].

There are several considerations for the design of Ti compounds for use in biomedical applications, among which are the microstructure, mainly the stabilization of the β-Ti phase, which favors a reduction in the Young's modulus [20,21]. Likewise, the β-Ti phase has been shown to have better performance against corrosion and wear than the α and α + β Ti alloys [22]. In Ti alloys, increasing alloying elements such as Nb, Zr, Cr, V, and Sn under certain cooling conditions can develop martensitic microstructures. The microstructure of Ti alloys largely depends on β-stabilizing elements. The β-Ti phase proceeds to decompose into two different types of martensite during the cooling process, from $\beta \rightarrow \alpha''$ (orthorhombic) and from $\beta \rightarrow \alpha'$ (hcp) [23,24]. These two types of martensite are considered the most important phases of Ti alloys because they possess super elastic properties that are ideal for applications in the biomedicine field [25].

Nb is an element that promotes the stabilization of the β-Ti phase and, in addition, reduces the Young's modulus to a value similar to that of human bone [26]. There are alloys of Ti with Nb that have low moduli when the β phase is stabilized, and a low concentration of Nb increases the probability of obtaining the α'-Ti martensitic phase [27,28], which has properties such as shape memory. In addition, Nb also promises to be a good element that, in combination with Ti alloys, promotes corrosion resistance [29,30] due to the formation of N_2O_5 oxide layers [31,32]. Finally, Nb is also used to replace vanadium (V) and aluminum (Al) in Ti alloys, which are potentially cytotoxic to the human body [33].

The present investigation shows the effects of adding Nb to the Ti matrix in parts manufactured by the powder metallurgy technique. A dilatometry study was conducted to observe the behavior of the Ti-xNb system during sintering. The microstructure was identified via X-ray diffraction (XRD) and scanning electron microscopy (SEM). Finally, the mechanical properties were obtained from simple compression tests.

2. Experimental Procedure

2.1. Sample Preparation

Ti metallic powders with particle sizes of less than 20 μm (d_{50} = 10.12 μm) and Nb powders with particle sizes of less than 100 μm (d_{50} = 34.05 μm) were obtained from Raymor, Boisbriand, QC, Canada and Sigma-Aldrich Co., St. Louis, MO, USA, Figure 1a and Figure 1b, respectively. Mixing of Ti with proportions of 5, 10, 15 and 20 wt.% Nb was carried out, and the mixture was bound to polyvinyl alcohol (PVA) [20]. The mixture was uniaxially compacted with a cylindrical steel die of 6 mm diameter with a pressure of 450 MPa.

2.2. Sintering Process

To eliminate the PVA, the specimen was first heated to 500 °C for 1800 s (30 min), and then the final sintering was carried out in a Lienseis L75V vertical dilatometer (Linseis, Robbinsville, NJ, USA) at 1260 °C with a heating rate of 0.416 °C/s (25 °C/min), which

was maintained for 3600 s (1 h), followed by cooling at a rate of 0.416 °C/s (25 °C/min). Both cycles were performed in a controlled argon atmosphere.

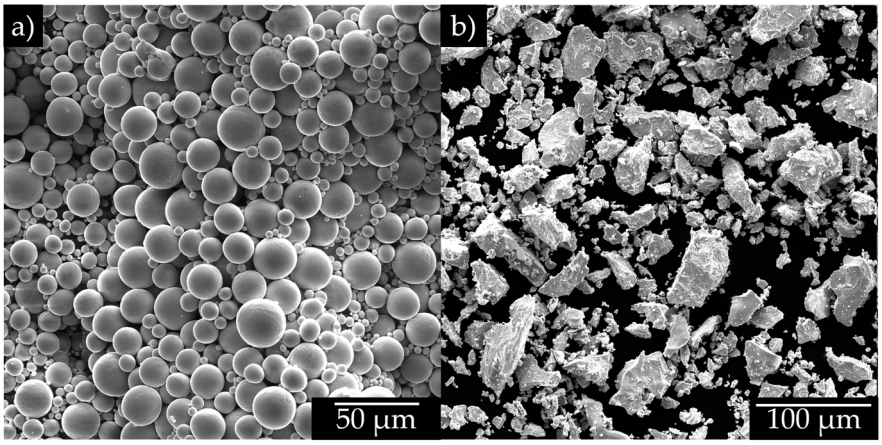

Figure 1. SEM images of (**a**) Ti and (**b**) Nb powders used for sample preparation.

2.3. Material Characterization

The sintered samples were prepared metallographically by roughing on silicon carbide (SiC) paper and polishing with alumina to a mirror finish. The microstructure was observed using a Tescan MIRA 3 LMU scanning electron microscope (FE-SEM TESCAN ORSAY HOLDING, a.s., Brno-Kohoutovice, Czech Republic). The diffraction patterns were obtained with a Bruker Siemens D500 diffractometer with an energy of 30 kV and a current of 30 mA at 2θ intervals of 30–80°.

2.4. Compression Tests

Simple uniaxial compression tests were carried out according to the ASTM D695-02 [34] standard with a head speed of 0.5 mm/min with an INSNTRON 1150 universal testing machine on cylindrical specimens with dimensions of 6 mm × 6 mm (height and diameter, respectively) at room temperature. The elastic moduli (E) were estimated from the stress-strain curves in the elastic zone after correction of the real data obtained.

2.5. Corrosion Test

To evaluate corrosion resistance, a standard three-electrode arrangement was used under the ASTM G3 standard [35], and the sintered samples were exposed to an electrolyte based on Hank's solution (HS) provided by Sigma Aldrich [25]. The tests were performed at an open circuit potential (OCP) for a 3000 s stay, and then a cathodic potential of −1.5 V was applied for 300 s to eliminate possible oxides formed during the OCP tests. Next, electrochemical impedance spectroscopy was evaluated with an amplitude from 10 mV against OCP in a frequency range of −0.01 Hz–100,000 Hz. Finally, potentiodynamic tests were performed from −0.3 V to 0.7 V with a saturated calomel electrode (SCE) and a scan of 0.01 mV/s. All tests were carried out at room temperature.

3. Results and Discussion

3.1. Dilatometry Analysis

The dilatometry study was carried out using the densities derived from the geometric dimensions and mass of the samples. Furthermore, the determination of the relative density depended on both the mass and the instantaneous volume during the entire sintering process, as dictated by the following equation:

$$D = \rho_i / \rho_T \quad (1)$$

where ρ represents the density and the subscripts i and T denote the instantaneous density and the total density of the compound comprising the sample. ρ_T is obtained using the rule of mixtures:

$$\rho_T = \rho_1 f_1 + \rho_2 f_2 \quad (2)$$

where ρ is the density and f indicates the mass fraction of the corresponding element, and the subscripts 1 and 2 represent the participating elements.

Furthermore, to obtain the instantaneous densification rate $\dot{D}$, it was estimated from the following differential equation:

$$\dot{D} = \frac{d\,\dot{D}_i}{dt_i} \quad (3)$$

where $\dot{D}$ represents the instantaneous densification at time t_i (s). More details on the procedure to determine the values from the dilatometry data can be found elsewhere [36].

The densification of the Ti-xNb compacts was evaluated during the sintering process (Figure 2). A graph of axial contraction as a function of time is presented, where it can be seen that the process consists of three stages. I—Expansion of the system until a change point indicates the beginning of sintering. II—A drop during heating to approximately 620 °C and a part of the isothermal process (1260 °C) indicate the axial contraction of the piece, and a negative value indicates that the sample suffers a volume contraction due to diffusion of the particles. III—Exponential behavior, where the contraction of the system reaches a maximum diffusion and the piece has no appreciable changes in its dimensions.

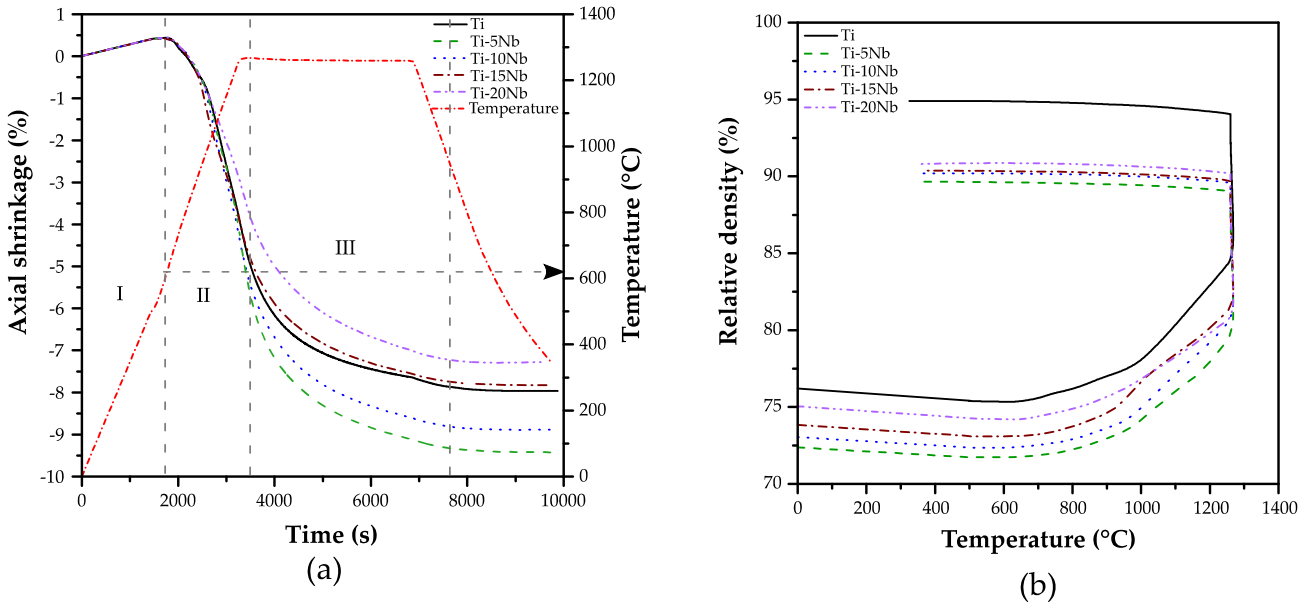

Figure 2. (**a**) Axial shrinkage as a function of temperature during the sintering process, (**b**) relative density as a function of temperature.

The addition of Nb to the pure Ti matrix generates significant changes in the final contraction that range from 7.2% to 9.4%. The largest change is recorded for the sample with a content of 5% Nb, and conversely, the smallest change occurs for the sample with 20% Nb. It can be seen that during the second stage of sintering, the pieces with 5–15% Nb had a similar contraction until reaching the change in slope. This behavior could indicate that sintering is carried out in almost the same way for these pieces, where there is more continuous diffusion of Nb particles in the Ti matrix. On the other hand, the highest percentage of Nb (20%) does not have a similarity with the aforementioned samples, which indicates that sintering caused changes in the interparticle diffusion process.

Once the third stage is reached, the contraction of each of the Ti-Nb systems is different, and the highest contraction is attributed to the lower content of Nb, which indicates that

the diffusion of Nb in the Ti matrix increases with decreasing content [37]. As the Nb concentration increases, the contraction decreases because the system begins to have a saturation of the element without diffusing; subsequently, an asymptotic behavior occurs, thus indicating that the sintering process is slightly slower after the end of the isothermal cycle at approximately 950 °C.

Figure 2b shows the change in relative density as a function of sintering temperature. The relative density tends to decrease as the Nb content increases. First, with pure Ti, a higher density is maintained since its particles are smaller and have a similar geometry, which allows better accommodation during compaction. Likewise, when Nb is added to the system, the irregular geometry and large particles rearrange the matrix in a manner that limits densification during the initial compaction process [38,39]. During heating, there is a slight decrease in density due to thermal expansion, up to approximately 620 °C. Likewise, when a temperature of 1260 °C is reached, the density increases until reaching the maximum value of densification; finally, there is a slight additional increase in densification due to thermal contraction during cooling [18].

The density changes are presented in Table 1. The final density of the compacts after the sintering cycle increases due to the increase in the amount of Nb since it has a density twice that of titanium (Nb = 8.57, Ti = 4.5 g/cm^3). Similarly, the relative density increases as the Nb content increases. Furthermore, after sintering, the relative density is maintained without a significant change. This behavior could be related to the diffusion of the Nb particles, where it decreases as the fraction of Nb in the Ti matrix increases [37], which limits the reduction in the volume of the material by having a greater amount of Nb without dissolving.

Table 1. Changes in the density after and before sintering.

	Ti	Ti-5Nb	Ti-10Nb	Ti-15Nb	Ti-20Nb
Theoretical density (g/cm^3)	4.5	4.70	4.90	5.11	5.31
Green density (g/cm^3)	3.43	3.34	3.45	3.57	3.73
Sintered density (g/cm^3)	4.27	4.13	4.26	4.37	4.41
Relative green density	0.762	0.724	0.730	0.738	0.750
Relative Sintered density	0.949	0.896	0.902	0.904	0.908
Contraction %	19.7	19.3	19.0	18.3	17.3

Figure 3 shows the densification rate as a function of temperature. There are several changes in densification that can be associated with the phase transitions that occur in the Ti-Nb system during continuous heating [40,41]. The first increase is registered at 613 °C, 566 °C and 622 °C for Ti, Ti-10Nb and Ti-20Nb, respectively, which is the starting point of sintering. Subsequently, the changes present a reaction with oxygen, phase transitions $\alpha \rightarrow \beta$, and finally the complete transformation to the β-Ti phase [20].

An increase in the quantity of Nb particles in the Ti matrix slightly decreased the phase transition temperature by approximately 3%, demonstrating that the addition of Nb favors a phase change with temperature smaller than that presented by pure Ti [42]. This behavior was also observed by Mi-Kyung Han via calorimetry tests [43]. Likewise, the change in the transition temperature is less than 1% between both systems with Nb, which indicates that the transformation temperature does not significantly change as the amount of Nb increases up to 20 wt.%. Finally, the changes in the densification rate become more constant as the Nb fraction increases; this could be because the system saturates quickly and the β-Ti phase is more easily reached.

3.2. Microstructural Analysis

The microstructure obtained after sintering for the different Nb contents is presented in Figure 4. Increasing the fraction of Nb in the Ti matrix also increased the amount of β-Ti phase obtained (clear phase), and there were also β-Ti-rich zones around the remaining Nb

particles (Figure 4a,b). As the amount of Nb increases in the system, diffusion becomes less evident due to the saturation of Nb in the Ti matrix (Figure 4c,d).

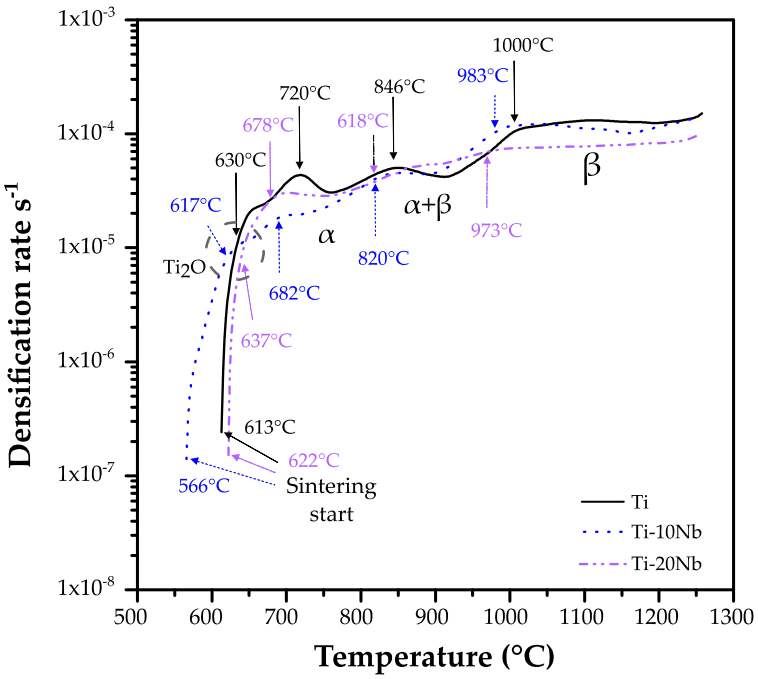

Figure 3. Densification rate during continuous heating at 1260 °C.

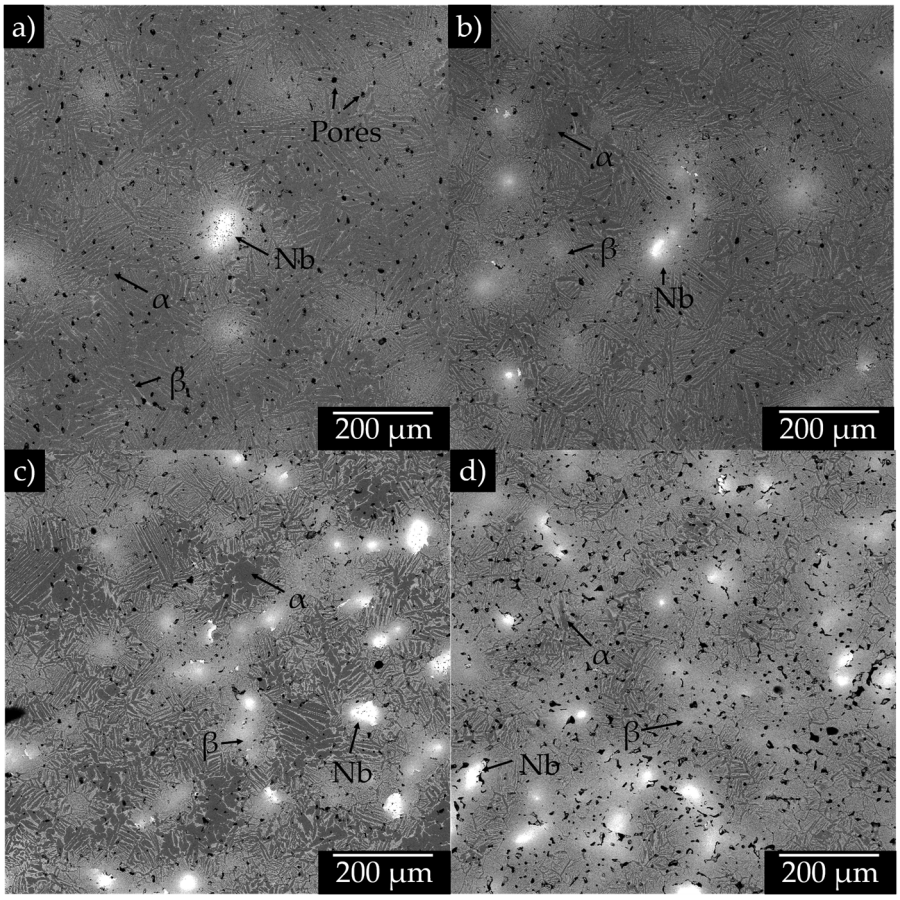

Figure 4. SEM images of the different Ti-Nb alloys with (**a**) 5%, (**b**) 10%, (**c**) 15% and (**d**) 20 wt.% of Nb.

Increasing the amount of Nb slightly increased the porosity of the matrix (Figure 4d), as described by Yunhui Chen et al. [44]. The residual porosity is favorable for a medical implant to have a greater chance of success because the adjacent tissue can have a more efficient anchorage [45].

Figure 5 shows the different magnifications used to observe the phases and morphologies that make up the microstructure of the sintered Ti-xNb pieces. It can be observed that around the Nb particle, there is a high concentration of the β-Ti phase; in addition, there are areas with the acicular α-Ti or α′-Ti phase (intercalated α and β lamellae). Figure 5b shows how the Nb particle begins to have an oval shape and loses the straight edges and original angles of these particles as the diffusion process occurs. More details of the diffusion process can be found in [44].

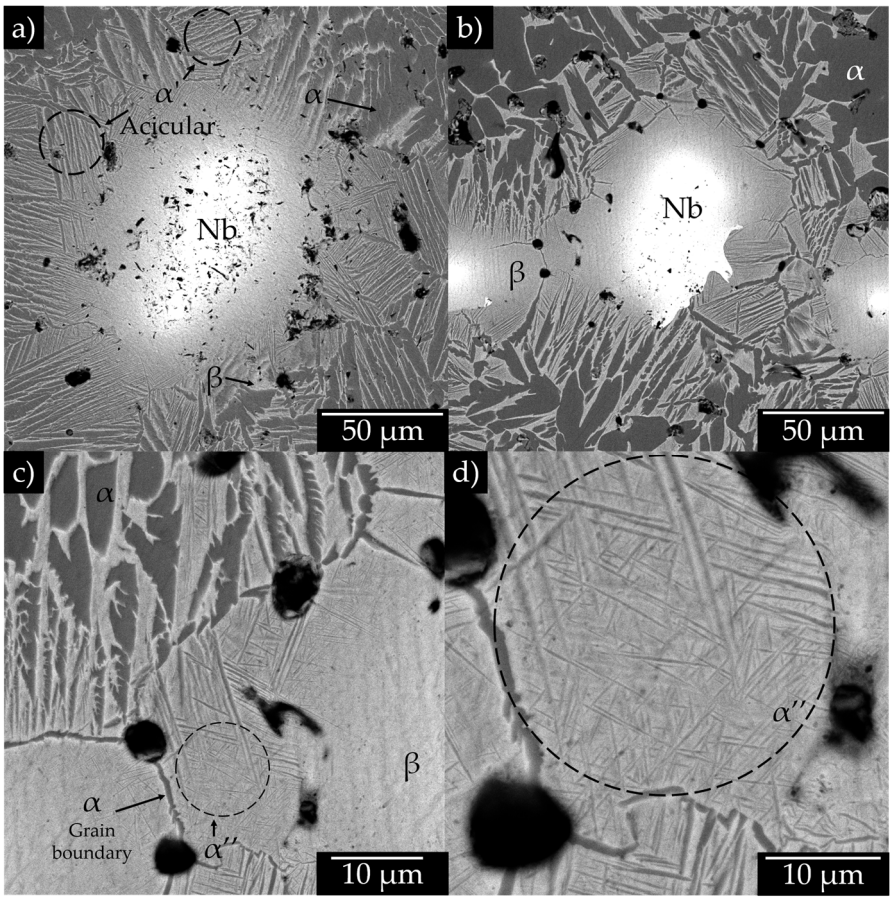

Figure 5. SEM images of the different sections of Ti-xNb samples with (**a**) 5 wt.% of Nb and (**b**–**d**) 15 wt.% of Nb showing martensite formation.

Figure 5c,d show how the α-Ti phase delimits the grain boundaries. Furthermore, within these phases, the martensitic α″-Ti phase can be observed, which is characterized by disordered needles, and this α′-Ti/α″-Ti microstructure becomes more predominant at 15% Nb or higher. The α′-Ti, α″-Ti and β-Ti phases help to reduce the Young modulus as well as the remaining porosity, which allows obtaining values close to those of human bones in comparison to the Ti alloys fabricated by casting [20,22,26]. In addition, it has been reported that the α″-Ti phase can present shape memory and superelasticity properties, which are favorable for medical applications [25].

It is possible that the formation of spontaneous oxides on the surface of these alloys could generate a bioinert layer when interacting with human body fluids. The generation of surface oxides could suppress the dissolution of Ti and Nb ions and, at the same time, determine the tissue–implant interaction. Jue Liu [11,46] demonstrated that the

presence of high Nb contents in Ti alloys favors the formation of apatite on the alloy surface. Furthermore, the presence of pores would also benefit the nucleation of these components in a human body fluid environment. The above results indicate that the presence of Nb particles that do not diffuse in their entirety in this study could be beneficial for promoting the apatite formation phenomena described above [47], in addition to increasing corrosion resistance [30].

The XRD patterns of Ti and the studied series of Ti-xNb alloys are presented in Figure 6. A complete α-Ti (hcp) structure is obtained for the Ti system without added Nb; once Nb is added to the matrix, the crystal structure changes. When the Nb content is greater than or less than 15 wt.%, a structure called α′-Ti (hexagonal) appears. It has been reported that with the addition of β-stabilizing elements, the martensitic structure distorts the hexagonal crystal structure [48,49]. When the Nb concentration is greater than 15 wt.%, the structure is mainly α″-Ti (orthorhombic), and the characteristic peaks of the α-Ti phase shift slightly to the right [49] (Figure 6b).

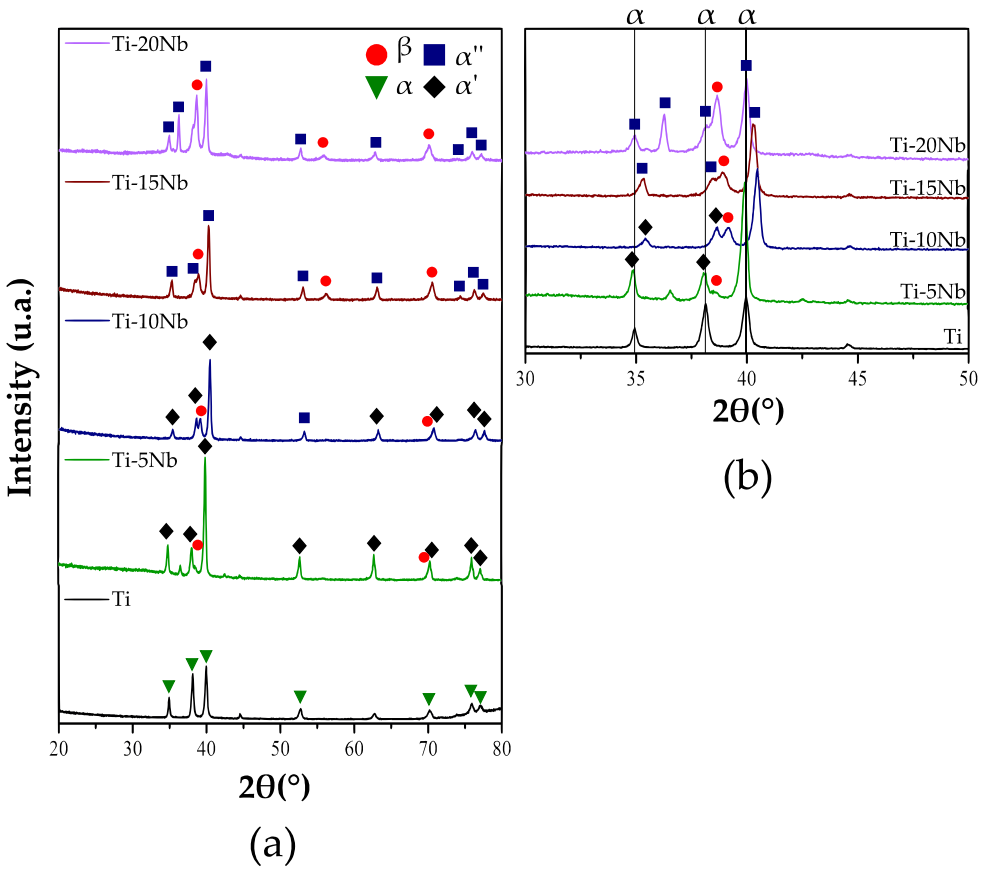

Figure 6. (**a**) XRD patterns and (**b**) close-up of the 30° to 50° patterns of the different samples of pure Ti and Ti-Nb after sintering.

J. Zhang et al. [24] demonstrated that the transformation of the β-Ti phase is primarily and preferably into α″-Ti. Furthermore, D'yakonova et al. [50] showed that the transformation of the predominant β-Ti phase from temperatures above 1100 °C first decomposes into the α″-Ti phase in Ti-Nb alloys. According to those studies, there is a high likelihood that with Nb concentrations favoring the stabilization of the β-Ti phase, where it predominates at temperatures above 1000 °C, primarily biphasic structures of β + α″ can be obtained.

In addition, when the amount of Nb exceeds 15 wt.%, the amount of β-Ti phase is increasingly evident, and at the same time, the martensitic faces of α-Ti (α′, α″) tend to decrease with increasing Nb [51]. The manufactured samples have a biphasic α + β structure where the β microstructure is the predominant phase [52,53]. The quantity of remaining Nb particles is not detected in the diffraction patterns. Similar results are

reported by Dapeng Zhao et al. [54], where the large Nb particles are not detected by XDR when the sintering temperature is higher than 1100 °C. In this case, the interaction between Nb and Ti is enough to stabilize the β-Ti phase with a body-centered cubic structure (BCC) formed around the Nb particles. This formation of the β-Ti phase limits the detection of the α-Nb phase, which also has a BCC structure.

3.3. Compression Analysis

The results of the compression test are presented in Figure 7a, and the Young's moduli are presented in Figure 7b. It can be observed that there is a decrease in the compressive strength as the Nb content in the matrix increases; this behavior is mainly due to the increase in the proportion of the β-Ti phase, where, in addition, the quantity of the α-Ti phase decreases, as explained in Figures 4–6. Likewise, there is a greater ductility when there is a greater proportion of Nb in the matrix, and we also remember that a higher % of Nb increases the porosity of the system, which also favors a decrease in the mechanical properties and increases ductility [55].

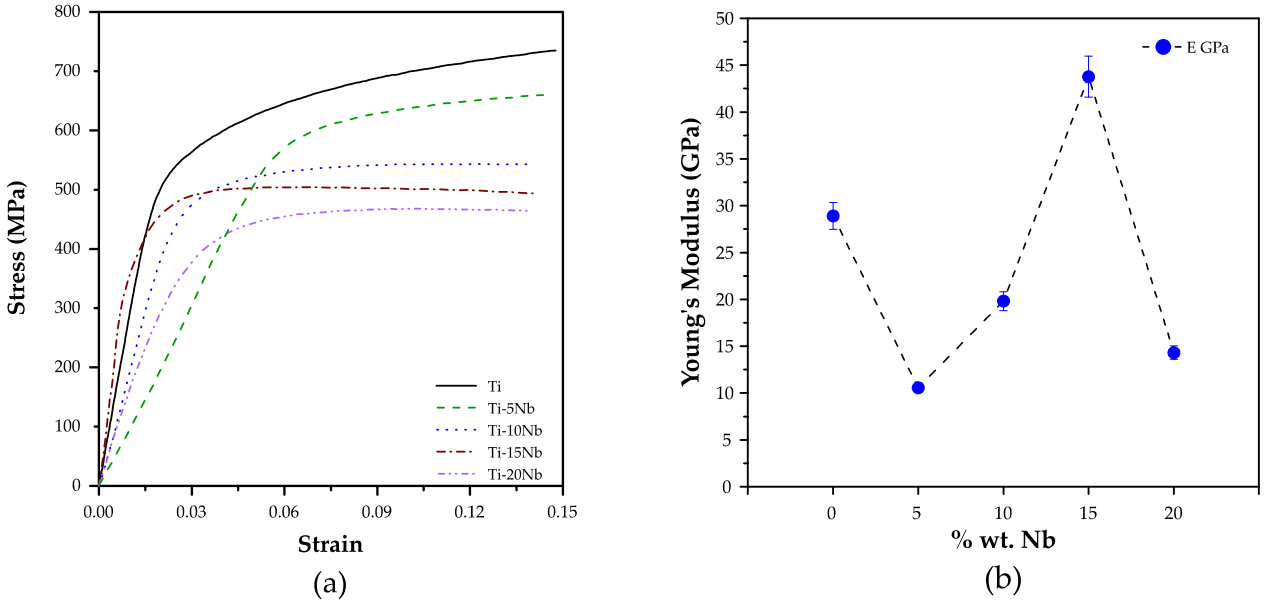

Figure 7. (**a**) Stress-strain graph and (**b**) Young's modulus of the Ti-xNb samples sintered at 1260 °C.

When evaluating the elastic limit (Figure 7b), there is a decrease in the modulus when Nb is added to the system. The increase in the modulus of the Ti-15Nb alloy is due to a combination of several factors, and this increase can be caused by deformation mechanisms, such as sliding, twinning and strain-induced transformations of the stabilized β-Ti alloys [44,56]. In addition, the contents of the α′-Ti and α″-Ti phases also affect the elastic modulus; as the proportion of α′-Ti increases, the modulus tends to decrease compared with that of the α phase of pure Ti, as is observed when comparing Ti with Ti-5Nb and Ti-10Nb [57]. Likewise, it is possible that the unsolved Nb particles increased the elastic modulus of Ti-10Nb and Ti-15Nb alloys. J.C. Wang [58–60] demonstrates that unsolved particles have higher Young's modulus values than those of the β phase of the Ti-Nb matrix, resulting in higher Young's moduli for Ti-Nb systems fabricated by powder mixtures. Finally, there is again a decrease in the elastic modulus for Ti-20Nb, which may be due to the high saturation of the β-Ti phase and the presence of greater porosity [20,43,44].

3.4. Electrochemical Behavior Study

The open circuit potential (OCP) curves of the Ti-xNb samples immersed in Hank's solution for 3000 s are shown in Figure 8. It can be observed that the specimens with Nb concentrations of 5, 15 and 20 wt.% have a positive displacement tendency until a

certain stability is reached. The trend of OCP values over time recorded for the Ti-Nb samples moves towards more positive values, indicating improved corrosion resistance performance. On the other hand, the sample with 10% by weight of Nb enters an anodic zone and shifts towards negative potentials until it stabilizes in behavior. This behavior suggests that a passive protective film formed on the surfaces of all the samples, remaining stable after 3000 s immersed in Hank's solution [61,62].

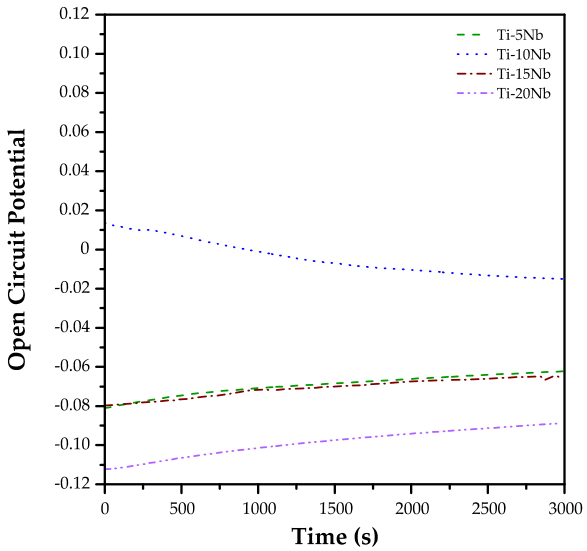

Figure 8. OCP–time plots of Ti-xNb alloys obtained in Hank's solution at 50 min.

Figure 9 shows the complementary Nyquist (Figure 9a) and Bode diagrams (Figure 9b) of the studied samples. Figure 9a shows that the specimens have a semicircle, with the Ti-15Nb electrode having the largest size, followed by the Ti-20Nb specimen. This suggests that they present greater resistance to corrosion than do the samples with lower Nb contents. According to the Bode diagram (Figure 9b), the specimens exhibit similar behavior at high frequencies, while a different behavior is observed at low frequencies. The Ti-15Nb sample exhibits superior corrosion resistance, as reflected by its higher impedance modulus |Z| at low frequencies. Conversely, the Ti-20Nb sample displays lower corrosion resistance due to its lower impedance modulus |Z| at low frequencies in comparison with Ti-15Nb [63]. This behavior can be explained by the porosity of the sample. Regarding the Bode plots, it can be observed that their shape appears to be influenced by the behavior of two time constants. This behavior is typically attributed to the formation of a passive layer on the surface of the pores, where metal–electrolyte interactions occur [64].

The behavior of the Ti-xNb systems was compared with that of the equivalent electrical circuit (CEE) to obtain the characteristic parameters of these tests, which are presented in Table 2. The CEE is composed of corrosion resistance followed by two parallel time constants. The first time constant considers the formation of an oxide on the surface of the Ti-xNb samples, which is composed of the resistance of the surface oxide formed (Ro) and the constant phase element (CP1) that considers the porosity obtained by the sintering process of the samples. Currently, there is an oxide layer both on the exterior surface and on the surface of the pores [65]. This is because oxide films have their own resistance or capacitance depending on where they are located. The second time constant is found in parallel and considers that the surface oxide layer may have greater corrosion resistance than inside the pores, represented by an additional resistance Rp and a capacitor (C1), as shown in Figure 9c. Similar models were used by Nikita Zaveri and A.C. Alves [61,63].

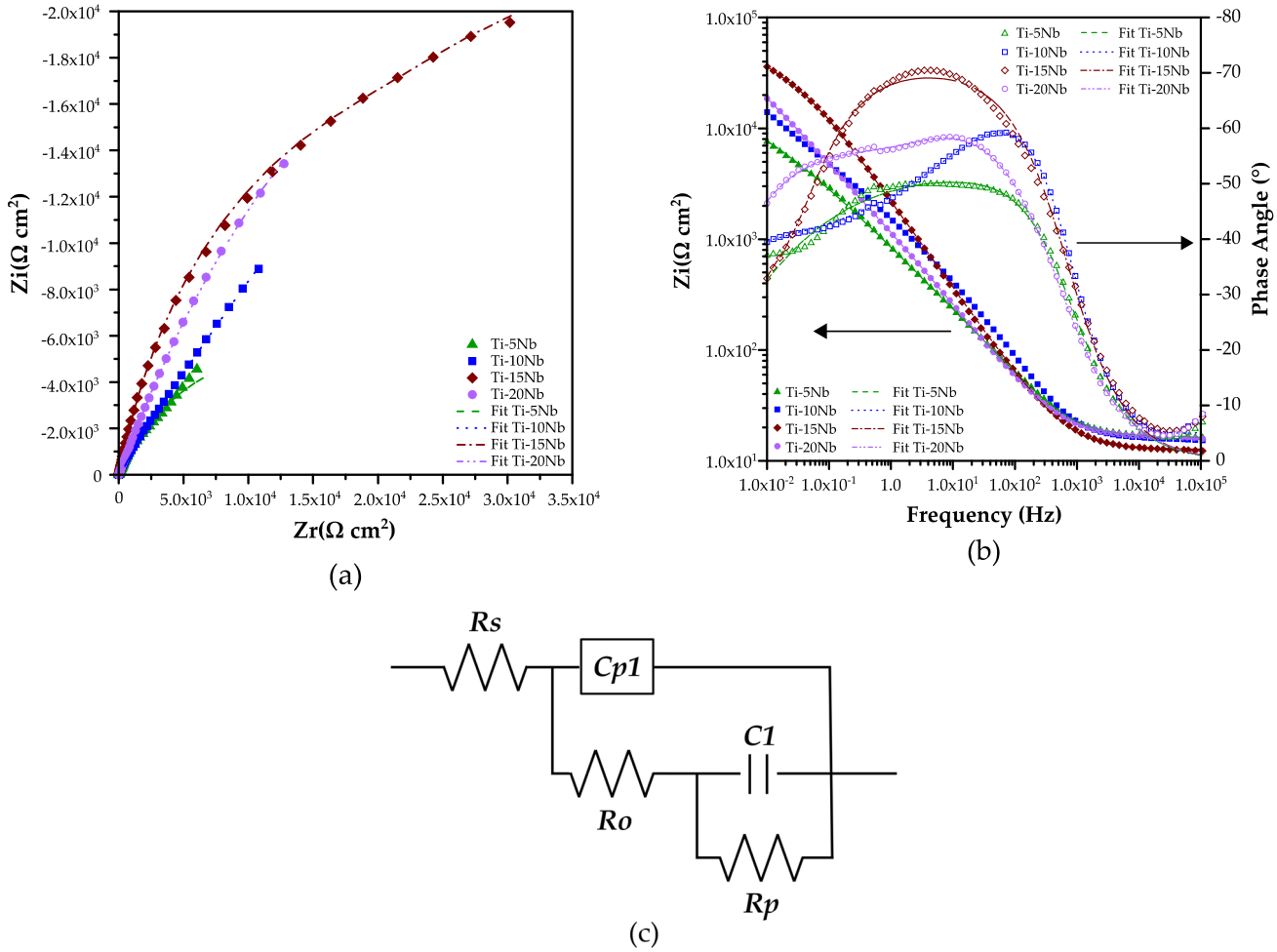

Figure 9. (**a**) Nyquist and (**b**) Bode plots of Ti-xNb alloys obtained in Hank's solution and (**c**) CEE for fitting and simulation of the electrochemical impedance spectroscopy experimental data.

Table 2. Equivalent electrical parameters obtained by fitting the experimental results of the Nyquist plots.

Sample	χ^2	Rs ($\Omega \cdot cm^2$)	CPE1-T ($F \cdot cm^{-2} \cdot s^{n-1}$)	CPE1-P	Ro ($\Omega \cdot cm^2$)	C1 ($F \cdot cm^{-2}$)	Rp ($\Omega \cdot cm^2$)
Ti-5Nb	1.32×10^{-3}	14.89	4.10×10^{-4}	0.5557	5.65	6.68×10^{-6}	18,730
Ti-10Nb	3.72×10^{-3}	16.53	2.13×10^{-4}	0.6716	15.89	8.93×10^{-6}	60,737
Ti-15Nb	3.15×10^{-3}	12.33	1.05×10^{-4}	0.7763	294.6	3.19×10^{-6}	47,541
Ti-20Nb	1.20×10^{-3}	15.23	2.66×10^{-4}	0.6338	8.22	6.52×10^{-6}	83,251

Figure 10 shows the potentiodynamic polarization curves of the Ti-xNb samples. The samples with Nb concentrations of 5, 10 and 15% present behaviors similar to each other, with a slight change toward more positive values of Ecorr and lower values of Icorr. In addition, it is clear that with a lower concentration of Nb, the corrosion process is most stable in the anodic dissolution zone [30].

An increase in the amount of Nb (10 and 15 wt.%) favors corrosion resistance because it presents a slightly lower Icorr than the other systems. By increasing the concentration up to 20 wt.%, there is a significant change in the behavior of this system, where Ecorr decreases compared to that of the other systems, from −0.20 V for Ti-10Nb to −0.38 V for Ti-20Nb, as presented in Table 3. This indicates that the corrosion capacity of this compound is diminished. The corrosion parameters are shown in Table 3. Compounds with concentrations greater than 10 wt.% of Nb have better resistance to corrosion, where 15 wt.% of Nb is considered to be the most resistant [66].

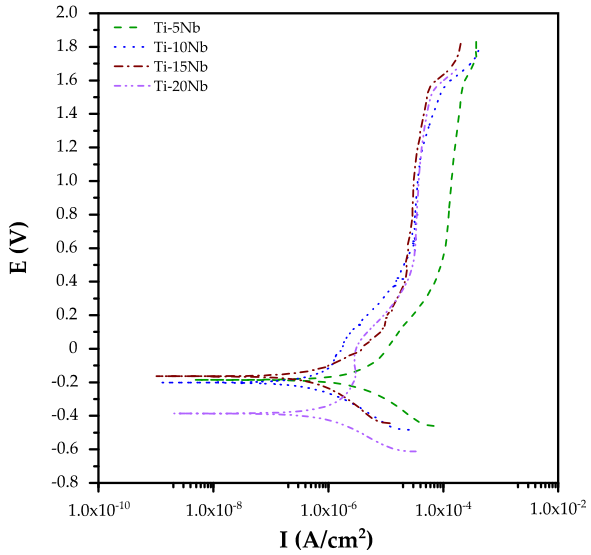

Figure 10. Potentiodynamic polarization curves of all the samples in Hank's solution.

Table 3. Tafel analysis results for the Ti-xNb samples in Hank's solution.

	Ti-5Nb	Ti-10Nb	Ti-15Nb	Ti-20Nb
Ba (mV)	461.05	1053.9	234.17	1276.2
Bc (mV)	273.31	272.31	285.73	307.08
Icorr (μA/cm^2)	4.7252	1.2475	0.7781	2.4642
Ecorr (mV)	−185.46	−201.98	−163.78	−386.15
Corr Rate (μm/Y)	100.15	23.345	14.161	42.867

The corrosion response improved with the addition of Nb and could be attributed again to the microstructure being rich in the β-Ti phase; this improved behavior is due to the surface oxides of Nb in the samples. Similar behavior was presented by R. Macias [29], where the addition of up to 20 wt.% Nb to Ti-Ta systems increased the corrosion resistance. Additionally, the porosity of the sample significantly impacts its corrosion resistance. This suggests that the surface pores and their geometry dictate how the material interacts with the electrolyte, potentially increasing its susceptibility to corrosion.

4. Conclusions

Based on the results obtained from the manufacturing of the Ti-xNb samples, the following conclusions can be drawn.

The dilatometry analysis showed that Nb affects the sintering behavior of the Ti matrix. In addition, the density of Nb and the fraction of Nb in the Ti matrix tend to generate a material with a lower relative density due to the increase in the porosity of the material after the sintering process. Likewise, Nb reduces the phase transition temperature of Ti but does not change the conditions with the addition of Nb up to 20 wt.%.

The characterization revealed that Nb stabilizes the β-Ti phase and at the same time favors the formation of the martensitic α′-Ti phase and, from 15% by weight, the α″-Ti phase. The formation of these martensite phases occurs after a relatively accelerated cooling in all samples, which occurs during the sintering process and Nb diffusion.

From the analysis of the mechanical behavior, it was determined that Nb significantly reduced the compressive behavior of the Ti matrix; in addition, it generated more ductile materials, although this can also be favored by the residual pores obtained after sintering. The Young's modulus also decreases compared to that of pure Ti, and at the same time, this property depends on the α-Ti and β-Ti phases obtained during cooling. The resulting value of the elastic modulus was lower than that of the materials manufactured by casting, which reached 60–80 GPa.

Finally, the corrosion behavior indicated that the corrosion resistance could depend more on the Ti phase present in the matrix than on the amount of alloying elements diffused into it. The corrosion test revealed that the samples with 10 and 15% Nb particles are the most promising because they are more resistant to the corrosion process, demonstrating that the proposed compounds can be a good alternative to Ti alloys for use in the medical field.

This is why the generation of materials composed of nontoxic elements and manufactured using the PM technique is a great alternative for obtaining parts that can be used in the field of medicine.

Author Contributions: Conceptualization, L.O. and R.M.J.; methodology, R.M.J.; project administration, P.G.G.; supervision, P.G.G. and J.A.Á.-O.; writing—original draft, formal analysis, L.O., R.M.J., F.A.-H. and I.A.-F.; investigation, L.O., R.M.J. and M.V.-P.; writing—review and editing, L.O., O.J., J.A.Á.-O. and F.A.-H.; validation, R.M.J. and M.V.-P.; visualization; image processing, L.O. and I.A.-F. All authors have read and agreed to the published version of the manuscript.

Funding: This research was supported by the National Council of Humanities, Science and Technology CONAHCYT during the postdoctoral stage of R. Macias and I. Alanis; grant numbers CVU 789772 and CVU 737815; and PhD. Stage of M. Velasco; grant number CVU 593226. The research was also supported by the scientific research coordination (CIC) of the UMSNH.

Institutional Review Board Statement: Not applicable.

Informed Consent Statement: Not applicable.

Data Availability Statement: Data are contained within the article.

Acknowledgments: The authors would like to thank to the Unidad Académica de Ingeniería I, Universidad Autónoma de Zacatecas, for the XRD data acquisition and processing.

Conflicts of Interest: The authors declare no conflicts of interest.

References

1. Zhang, E.; Zhao, X.; Hu, J.; Wang, R.; Fu, S.; Qin, G. Antibacterial metals and alloys for potential biomedical implants. *Bioact. Mater.* **2021**, *6*, 2569–2612. [CrossRef] [PubMed]
2. Cui, Y.-W.; Wang, L.; Zhang, L.-C. Towards load-bearing biomedical titanium-based alloys: From essential requirements to future developments. *Prog. Mater. Sci.* **2024**, *144*, 101277. [CrossRef]
3. Zhou, Y.-L.; Niinomi, M.; Akahori, T. Changes in mechanical properties of Ti alloys in relation to alloying additions of Ta and Hf. *Mater. Sci. Eng. A* **2008**, *483–484*, 153–156. [CrossRef]
4. Zhou, Y.L.; Niinomi, M.; Akahori, T. Effects of Ta content on Young's modulus and tensile properties of binary Ti–Ta alloys for biomedical applications. *Mater. Sci. Eng. A* **2004**, *371*, 283–290. [CrossRef]
5. Gupta, A.; Khatirkar, R.; Singh, J. A review of microstructure and texture evolution during plastic deformation and heat treatment of β-Ti alloys. *J. Alloys Compd.* **2022**, *899*, 163242. [CrossRef]
6. Long, M.; Rack, H.J. Titanium alloys in total joint replacement—A materials science perspective. *Biomaterials* **1998**, *19*, 1621–1639. [CrossRef] [PubMed]
7. Zhou, Z.; Liu, X.; Liu, Q.; Liu, L. Evaluation of the potential cytotoxicity of metals associated with implanted biomaterials (I). *Prep. Biochem. Biotechnol.* **2008**, *39*, 81–91. [CrossRef] [PubMed]
8. Niinomi, M. Recent metallic materials for biomedical applications. *Metall. Mater. Trans. A* **2002**, *33*, 477–486. [CrossRef]
9. Bolzoni, L.; Ruiz-Navas, E.M.; Gordo, E. Evaluation of the mechanical properties of powder metallurgy Ti-6Al-7Nb alloy. *J. Mech. Behav. Biomed. Mater.* **2017**, *67*, 110–116. [CrossRef]
10. Zhang, W.; Liu, Y.; Li, H.Z.; Li, Z.; Wang, H.J.; Liu, B. Constitutive modeling and processing map for elevated temperature flow behaviors of a powder metallurgy titanium aluminide alloy. *J. Mater. Process. Technol.* **2009**, *209*, 5363–5370. [CrossRef]
11. Liu, J.; Chang, L.; Liu, H.; Li, Y.; Yang, H.; Ruan, J. Microstructure, mechanical behavior and biocompatibility of powder metallurgy Nb-Ti-Ta alloys as biomedical material. *Mater. Sci. Eng. C* **2017**, *71*, 512–519. [CrossRef] [PubMed]
12. Chen, Q.; Thouas, G.A. Metallic implant biomaterials. *Mater. Sci. Eng. R Rep.* **2015**, *87*, 1–57. [CrossRef]
13. Anene, F.A.; Aiza Jaafar, C.N.; Zainol, I.; Azmah Hanim, M.A.; Suraya, M.T. Biomedical materials: A review of titanium-based alloys. *Proc. Inst. Mech. Eng. Part C J. Mechan. Eng. Sci.* **2021**, *235*, 3792–3805. [CrossRef]
14. Wang, X.; Xu, S.; Zhou, S.; Xu, W.; Leary, M.; Choong, P.; Qian, M.; Brandt, M.; Xie, Y.M. Topological design and additive manufacturing of porous metals for bone scaffolds and orthopedic implants: A review. *Biomaterials* **2016**, *83*, 127–141. [CrossRef] [PubMed]
15. Amigó, V.; Salvador, M.D.; Romero, F.; Solves, C.; Moreno, J.F. Microstructural evolution of Ti–6Al–4V during the sintering of microspheres of Ti for orthopedic implants. *J. Mater. Process. Technol.* **2003**, *141*, 117–122. [CrossRef]

16. Bellemans, J. Osseointegration in porous coated knee arthroplasty: The influence of component coating type in sheep. *Acta Orthop.* **1999**, *70* (Suppl. 288), i-35. [CrossRef]
17. Oh, I.-H.; Nomura, N.; Masahashi, N.; Hanada, S. Mechanical properties of porous titanium compacts prepared by powder sintering. *Scr. Mater.* **2003**, *49*, 1197–1202. [CrossRef]
18. Cabezas-Villa, J.L.; Olmos, L.; Bouvard, D.; Lemus-Ruiz, J.; Jiménez, O. Processing and properties of highly porous Ti6Al4V mimicking human bones. *J. Mater. Res.* **2018**, *33*, 650–661. [CrossRef]
19. Dudina, D.V.; Bokhonov, B.B.; Olevsky, E.A. Fabrication of porous materials by spark plasma sintering: A review. *Materials* **2019**, *12*, 541. [CrossRef]
20. Macias, R.; Garnica-Gonzalez, P.; Olmos, L.; Jimenez, O.; Chavez, J.; Vazquez, O.; Alvarado-Hernandez, F.; Arteaga, D. Sintering Analysis of Porous Ti/xTa Alloys Fabricated from Elemental Powders. *Materials* **2022**, *15*, 6548. [CrossRef]
21. Niinomi, M. Fatigue performance and cyto-toxicity of low rigidity titanium alloy, Ti–29Nb–13Ta–4.6Zr. *Biomaterials* **2003**, *24*, 2673–2683. [CrossRef]
22. Filip, R.; Kubiak, K.; Ziaja, W.; Sieniawski, J. The effect of microstructure on the mechanical properties of two-phase titanium alloys. *J. Mater. Process. Technol.* **2003**, *133*, 84–89. [CrossRef]
23. Motyka, M. Martensite formation and decomposition during traditional and AM processing of two-phase titanium alloys—An overview. *Metals* **2021**, *11*, 481. [CrossRef]
24. Zhang, J.; Tasan, C.C.; Lai, M.J.; Dippel, A.-C.; Raabe, D. Complexion-mediated martensitic phase transformation in Titanium. *Nat. Commun.* **2017**, *8*, 14210. [CrossRef]
25. Li, P.; Ma, X.; Wang, D.; Zhang, H. Microstructural and mechanical properties of β-type Ti–Nb–Sn biomedical alloys with low elastic modulus. *Metals* **2019**, *9*, 712. [CrossRef]
26. Karre, R.; Niranjan, M.K.; Dey, S.R. First principles theoretical investigations of low Young's modulus beta Ti–Nb and Ti–Nb–Zr alloys compositions for biomedical applications. *Mater. Sci. Eng. C* **2015**, *50*, 52–58. [CrossRef]
27. Zhuravleva, K.; Bönisch, M.; Scudino, S.; Calin, M.; Schultz, L.; Eckert, J.; Gebert, A. Phase transformations in ball-milled Ti–40Nb and Ti–45Nb powders upon quenching from the ß-phase region. *Powder Technol.* **2014**, *253*, 166–171. [CrossRef]
28. Zhao, X.-Y.; Chen, R.-R.; Yang, Y.; Guo, J.-J.; Ding, H.-S.; Su, Y.-Q.; Fu, H.-Z. Microstructure and mechanical properties of Ti43Al6Nb alloys with different zirconium contents. *Rare Met.* **2023**, *42*, 2047–2056. [CrossRef]
29. Macias, R.; Garnica-Gonzalez, P.; Villalobos-Brito, J.; Fernandez-Salvador, C.; Alanis-Fuerte, I.; Olmos, L.; Jimenez, O.; Chávez, J. Effect of niobium on corrosion resistance of 75Ti-x-25Ta-xNb alloy. *MRS Adv.* **2024**, 1–4. [CrossRef]
30. Singh, N.; Srikanth, K.P.; Gopal, V.; Rajput, M.; Manivasagam, G.; Prashanth, K.G.; Chatterjee, K.; Suwas, S. In Situ Production of Low-Modulus Ti-Nb Alloys by Selective Laser Melting and their Functional Assessment Toward Orthopedic Applications. *J. Mater. Chem. B* **2024**, *12*, 5982–5993. [CrossRef]
31. Vishnu, D.S.M.; Sure, J.; Liu, Y.; Kumar, R.V.; Schwandt, C. Electrochemical synthesis of porous Ti-Nb alloys for biomedical applications. *Mater. Sci. Eng. C* **2019**, *96*, 466–478. [CrossRef] [PubMed]
32. Vishnu, D.S.M.; Sure, J.; Schwandt, C. Effect of Nb on phase composition, microstructure and corrosion resistance of electrochemically synthesized porous Ti-xNb-13Zr for use as a bioalloy. *J. Alloy. Met. Syst.* **2024**, *6*, 100072. [CrossRef]
33. Sarraf, M.; Rezvani Ghomi, E.; Alipour, S.; Ramakrishna, S.; Liana Sukiman, N. A state-of-the-art review of the fabrication and characteristics of titanium and its alloys for biomedical applications. *Bio-Des. Manuf.* **2021**, *5*, 371–395. [CrossRef] [PubMed]
34. *ASTM D695-02*; Standard Test Method for Compressive Properties of Rigid Plastics. ASTM: West Conshohocken, PA, USA, 2017.
35. *ASTM G3-89*; Standard Practice for Conventions Applicable to Electrochemical Measurements in Corrosion Testing. ASTM: West Conshohocken, PA, USA, 2010.
36. Mihalcea, E.; Hernández, H.V.; Olmos, L.; Jimenez, O. Semi-solid sintering of Ti6Al4V/CoCrMo composites for biomedical applications. *Mater. Res.* **2019**, *22*, e20180391. [CrossRef]
37. Pontau, A.E.; Lazarus, D. Diffusion of titanium and niobium in bcc Ti-Nb alloys. *Phys. Rev. B* **1979**, *19*, 4027. [CrossRef]
38. Panelli, R.; Ambrozio Filho, F. A study of a new phenomenological compacting equation. *Powder Technol.* **2001**, *114*, 255–261. [CrossRef]
39. Heckel, R.W. Density-pressure relationships in powder compaction. *Trans. Metal. Soc. AIME* **1961**, *221*, 671–675.
40. Hui, Q.; Xue, X.; Kou, H.; Lai, M.; Tang, B.; Li, J. Kinetics of the ω phase transformation of Ti-7333 titanium alloy during continuous heating. *J. Mater. Sci.* **2013**, *48*, 1966–1972. [CrossRef]
41. Alanis-Fuerte, I.; Garnica-González, P.; López-Martínez, E.; Vergara-Hernández, H.J.; Vázquez-Gómez, O. Effect of Cold-rolling and Heating Rate on Austenite Formation in a Low–Carbon Steel. *ISIJ Int.* **2022**, *62*, 227–236. [CrossRef]
42. Moffat, D.L.; Kattner, U.R. The stable and metastable Ti-Nb phase diagrams. *Metall. Trans. A* **1998**, *19*, 2389–2397. [CrossRef]
43. Han, M.-K.; Kim, J.-Y.; Hwang, M.-J.; Song, H.-J.; Park, Y.-J. Effect of Nb on the microstructure, mechanical properties, corrosion behavior, and cytotoxicity of Ti-Nb alloys. *Materials* **2015**, *8*, 5986–6003. [CrossRef] [PubMed]
44. Chen, Y.; Han, P.; Dehghan-Manshadi, A.; Kent, D.; Ehtemam-Haghighi, S.; Jowers, C.; Bermingham, M.; Li, T.; Cooper-White, J.; Dargusch, M.S. Sintering and biocompatibility of blended elemental Ti-xNb alloys. *J. Mech. Behav. Biomed. Mater.* **2020**, *104*, 103691. [CrossRef] [PubMed]
45. Zheng, Y.; Han, Q.; Wang, J.; Li, D.; Song, Z.; Yu, J. Promotion of osseointegration between implant and bone interface by titanium alloy porous scaffolds prepared by 3D printing. *ACS Biomater. Sci. Eng.* **2020**, *6*, 5181–5190. [CrossRef] [PubMed]

46. Liu, J.; Ruan, J.; Chang, L.; Yang, H.; Ruan, W. Porous Nb-Ti-Ta alloy scaffolds for bone tissue engineering: Fabrication, mechanical properties and in vitro/vivo biocompatibility. *Mater. Sci. Eng. C* **2017**, *78*, 503–512. [CrossRef] [PubMed]
47. Farrahnoor, A.; Zuhailawati, H. Effects of hydroxyapatite addition on the bioactivity of Ti-Nb alloy matrix composite fabricated via powder metallurgy process. *Mater. Today Commun.* **2021**, *27*, 102209. [CrossRef]
48. Welsch, G.; Boyer, R.; Collings, E.W. (Eds.) *Materials Properties Handbook: Titanium Alloys*; ASM International: Novelty, OH, USA, 1993.
49. Moreno, J.G.; Bönisch, M.; Panagiotopoulos, N.T.; Calin, M.; Papageorgiou, D.G.; Gebert, A.; Eckert, J.; Evangelakis, G.A.; Lekka, C.E. Ab initio and experimental study of phase stability of Ti-Nb alloys. *J. Alloys Compd.* **2017**, *696*, 481–489. [CrossRef]
50. D'yakonova, N.B.; Lyasotskii, I.V.; Rodionov, Y.L. Orthorhombic martensite and the ω phase in quenched and deformed titanium alloys with 20–24 at% Nb. *Russ. Metall. Met.* **2007**, *2007*, 51–58. [CrossRef]
51. Marczewski, M.; Wieczerzak, K.; Maeder, X.; Lapeyre, L.; Hain, C.; Jurczyk, M.; Nelis, T. Microstructure and mechanical properties of Ti-Nb alloys: Comparing conventional powder metallurgy, mechanical alloying, and high-power impulse magnetron sputtering processes for supporting materials screening. *J. Mater. Sci.* **2024**, *59*, 9107–9125. [CrossRef]
52. Zhang, Y.; Liu, H.; Jin, Z. Thermodynamic assessment of the Nb-Ti system. *Calphad* **2001**, *25*, 305–317. [CrossRef]
53. Surmeneva, M.A.; Koptyug, A.; Khrapov, D.; Ivanov, Y.F.; Mishurova, T.; Evsevleev, S.; Prymak, O.; Loza, K.; Epple, M.; Bruno, G.; et al. In situ synthesis of a binary Ti–10at% Nb alloy by electron beam melting using a mixture of elemental niobium and titanium powders. *J. Mater. Process. Technol.* **2020**, *282*, 116646. [CrossRef]
54. Zhao, D.; Chang, K.; Ebel, T.; Nie, H.; Willumeit, R.; Pyczak, F. Sintering behavior and mechanical properties of a metal injection molded Ti–Nb binary alloy as biomaterial. *J. Alloys Compd.* **2015**, *640*, 393–400. [CrossRef]
55. Garnica, P.; Macías, R.; Chávez, J.; Bouvard, D.; Jiménez, O.; Olmos, L.; Arteaga, D. Fabrication and characterization of highly porous Ti6Al4V/xTa composites for orthopedic applications. *J. Mater. Sci.* **2020**, *55*, 16419–16431. [CrossRef]
56. Kent, D.; Wang, G.; Dargusch, M. Effects of phase stability and processing on the mechanical properties of Ti–Nb based β Ti alloys. *J. Mech. Behav. Biomed. Mater.* **2013**, *28*, 15–25. [CrossRef] [PubMed]
57. Lee, C.M.; Ju, C.P.; Chern Lin, J.H. Structure–property relationship of cast Ti–Nb alloys. *J. Oral Rehabil.* **2002**, *29*, 314–322. [CrossRef] [PubMed]
58. Wang, J.; Liu, Y.; Rabadia, C.D.; Liang, S.-X.; Sercombe, T.B.; Zhang, L.-C. Microstructural homogeneity and mechanical behavior of a selective laser melted Ti-35Nb alloy produced from an elemental powder mixture. *J. Mater. Sci. Technol.* **2021**, *61*, 221–233. [CrossRef]
59. Wang, J.C.; Liu, Y.J.; Liang, S.X.; Zhang, Y.S.; Wang, L.Q.; Sercombe, T.B.; Zhang, L.C. Comparison of microstructure and mechanical behavior of Ti-35Nb manufactured by laser powder bed fusion from elemental powder mixture and prealloyed powder. *J. Mater. Sci. Technol.* **2022**, *105*, 1–16. [CrossRef]
60. Wang, J.C.; Liu, Y.J.; Qin, P.; Liang, S.X.; Sercombe, T.B.; Zhang, L.C. Selective laser melting of Ti–35Nb composite from elemental powder mixture: Microstructure, mechanical behavior and corrosion behavior. *Mater. Sci. Eng. A* **2019**, *760*, 214–224. [CrossRef]
61. Zaveri, N.; Mahapatra, M.; Deceuster, A.; Peng, Y.; Li, L.; Zhou, A. Corrosion resistance of pulsed laser-treated Ti–6Al–4V implant in simulated biofluids. *Electrochim. Acta* **2008**, *53*, 5022–5032. [CrossRef]
62. Chen, X.; Fu, Q.; Jin, Y.; Li, M.; Yang, R.; Cui, X.; Gong, M. In vitro studying corrosion behavior of porous titanium coating in dynamic electrolyte. *Mater. Sci. Eng. C* **2017**, *70*, 1071–1075. [CrossRef]
63. Alves, A.C.; Sendão, I.; Ariza, E.; Toptan, F.; Ponthiaux, P.; Pinto, A.M.P. Corrosion behaviour of porous Ti intended for biomedical applications. *J. Porous Mater.* **2016**, *23*, 1261–1268. [CrossRef]
64. Ureña, J.; Tsipas, S.; Pinto, A.M.; Toptan, F.; Gordo, E.; Jiménez-Morales, A. Corrosion and tribocorrosion behaviour of β-type Ti-Nb and Ti-Mo surfaces designed by diffusion treatments for biomedical applications. *Corros. Sci.* **2018**, *140*, 51–60. [CrossRef]
65. Barcia, O.E.; D'Elia, E.; Frateur, I.; Mattos, O.R.; Pébère, N.; Tribollet, B. Application of the impedance model of de Levie for the characterization of porous electrodes. *Electrochim. Acta* **2002**, *47*, 2109–2116. [CrossRef]
66. Chen, Y.-I.; Chen, Y.-J.; Lai, C.-Y.; Chang, L.-C. Mechanical and anticorrosive properties of TiNbTa and TiNbTaZr films on Ti-6Al-4V alloy. *Coatings* **2022**, *12*, 1985. [CrossRef]